

Article

Deriving Total Suspended Matter Concentration from the Near-Infrared-Based Inherent Optical Properties over Turbid Waters: A Case Study in Lake Taihu

Wei Shi ^{1,2,*} , Yunlin Zhang ³  and Menghua Wang ¹ 

¹ National Oceanic and Atmospheric Administration, National Environmental Satellite, Data, and Information Service, Center for Satellite Applications and Research, E/RA3, 5830 University Research Ct., College Park, MD 20740, USA; Menghua.Wang@noaa.gov

² Cooperative Institute for Research in the Atmosphere at Colorado State University, Fort Collins, CO 80523, USA

³ State Key Laboratory of Lake Science and Environment, Nanjing Institute of Geography and Limnology, Chinese Academy of Sciences, Nanjing 210008, China; ylzhang@niglas.ac.cn

* Correspondence: wei.1.shi@noaa.gov; Tel.: +1-301-683-3323; Fax: +1-301-683-3301

Received: 11 January 2018; Accepted: 14 February 2018; Published: 23 February 2018

Abstract: Normalized water-leaving radiance spectra $nL_w(\lambda)$, particle backscattering coefficients $b_{bp}(\lambda)$ in the near-infrared (NIR) wavelengths, and total suspended matter (TSM) concentrations over turbid waters are analytically correlated. To demonstrate the use of $b_{bp}(\lambda)$ in the NIR wavelengths in coastal and inland waters, we used in situ optics and TSM data to develop two TSM algorithms from measurements of the Visible Infrared Imaging Radiometer Suite (VIIRS) onboard the Suomi National Polar-orbiting Partnership (SNPP) using backscattering coefficients at the two NIR bands $b_{bp}(745)$ and $b_{bp}(862)$ for Lake Taihu. The correlation coefficients between the modeled TSM concentrations from $b_{bp}(745)$ and $b_{bp}(862)$ and the in situ TSM are 0.93 and 0.92, respectively. A different in situ dataset acquired between 2012 and 2016 for Lake Taihu was used to validate the performance of the NIR TSM algorithms for VIIRS-SNPP observations. TSM concentrations derived from VIIRS-SNPP observations with these two NIR $b_{bp}(\lambda)$ -based TSM algorithms matched well with in situ TSM concentrations in Lake Taihu between 2012 and 2016. The normalized root mean square errors (NRMSEs) for the two NIR algorithms are 0.234 and 0.226, respectively. The two NIR-based TSM algorithms are used to compute the satellite-derived TSM concentrations to study the seasonal and interannual variability of the TSM concentration in Lake Taihu between 2012 and 2016. In fact, the NIR-based TSM algorithms are analytically based with minimal in situ data to tune the coefficients. They are not sensitive to the possible $nL_w(\lambda)$ saturation in the visible bands for highly turbid waters, and have the potential to be used for estimation of TSM concentrations in turbid waters with similar NIR $nL_w(\lambda)$ spectra as those in Lake Taihu.

Keywords: VIIRS; Lake Taihu; TSM concentration; satellite ocean color; inherent optical property; turbid waters

1. Introduction

Total suspended matter (TSM) is an important biogeochemical parameter for both the ocean environment and inland waters. It can significantly impact the light fields in the water column, and consequently affect water optical and biological properties, such as the diffuse attenuation coefficient at the wavelength of 490 nm $K_d(490)$ [1–3], chlorophyll-a (Chl-a) concentration [4–6], and primary production [7,8], etc. TSM is also an indicator of water quality and water clarity that can affect both aquatic life and the lives of millions of people near coastal and inland waters. Changes in TSM concentrations are also related to the different atmosphere, land, and ocean processes, such as

river runoff and discharge [9,10], landslides and erosion [11], hurricanes and tropical storms [12–14], and ocean tidal currents [15,16].

In recent years, satellite ocean color remote sensing has been increasingly used to study ocean optical, biological, and biogeochemical processes, as well as to monitor for natural hazards in the world's open oceans and coastal and inland waters. Several algorithms have already been developed to derive the TSM concentration from satellite-measured normalized water-leaving radiance spectra $nL_w(\lambda)$. Specifically, $nL_w(\lambda)$ at the wavelength of 645 nm from the Moderate Resolution Imaging Spectroradiometer (MODIS) can be used to map TSM concentrations [17]. Remote sensing reflectance retrievals at wavelengths of 545 and 840 nm from Satellite Pour l'Observation de la Terre (SPOT) data have been used to quantify the TSM concentration [18]. Using MODIS-Aqua measurements, Son and Wang [19] developed a TSM algorithm for Chesapeake Bay using the strong relationship between TSM and the water diffuse attenuation coefficient at 490 nm ($K_d(490)$). Tassan [20] computed TSM using remote sensing reflectance at wavelengths of 488, 555, and 645 nm from Landsat Thematic Mapper (TM) data, and it was further tuned for MODIS observations in the Yellow Sea and East China Sea [21]. Other TSM algorithms, which are empirically tuned with different statistical approaches, were also developed for the Yellow Sea and East China Sea [22,23].

In general, our knowledge of the optical features in the red (~620–700 nm), near-infrared (NIR, ~700–1000 nm), and shortwave infrared (SWIR, ~1000–3000 nm) wavelengths for the coastal and inland waters is still quite limited, particularly for optical information at the NIR and SWIR wavelengths. Though, the optical information in the red, NIR, and SWIR can be used to derive a variety of ocean (water) products in turbid coastal and inland waters to address dynamic coastal ocean and inland water environments [24–27].

The water inherent optical properties (IOPs) are important parameters of the absorption and scattering of the constituents in the water column, i.e., pure water, phytoplankton, color dissolved organic matter (CDOM), and minerals, etc. It is well known that $nL_w(\lambda)$ spectra are determined by IOPs, such as absorption and backscattering of different bio-physical components in the water column [28]. Thus, IOPs can be derived using $nL_w(\lambda)$ spectra from satellite remote sensing [29–31]. However, most of these studies are focused on open ocean and less turbid waters. In fact, only $nL_w(\lambda)$ spectra in the visible are used in these IOP retrieval algorithms. The performance of these algorithms is poor in turbid coastal and inland waters since the coefficients for IOP spectral relations are empirical and normally tuned for open oceans or less turbid waters. In addition, the saturation of $nL_w(\lambda)$ in the visible wavelengths [32,33] in the highly turbid waters also indicates that IOP retrievals with $nL_w(\lambda)$ in the visible wavelengths can lead to significant underestimation of IOPs. Recently, improvements were also made to tune these algorithms with the in situ $nL_w(\lambda)$ in the NIR wavelengths in some regional studies [34–36].

In turbid coastal and inland waters, the backscattering coefficient $b_{bp}(\lambda)$ is generally proportional to the TSM concentration, thus deriving $b_{bp}(\lambda)$ becomes a prerequisite for any IOP-based TSM algorithm. In the visible wavelengths, the absorption and backscattering of all four constituents in the water column are significant in determining the $nL_w(\lambda)$ spectra. This makes it very challenging to accurately derive IOP properties from satellite-measured $nL_w(\lambda)$ spectra with visible bands in the coastal and inland waters. However, at the NIR wavelengths, the water absorption coefficients [37,38] are much larger than those of other components, such as phytoplankton, sediments, and CDOM. Thus, IOP models at the NIR wavelengths can be significantly simplified for turbid coastal and inland waters [33]. Indeed, Shi and Wang [33] have shown that backscattering coefficients $b_{bp}(\lambda)$ at the MODIS NIR bands can be analytically derived with good accuracy at the NIR and visible wavelengths in coastal and inland waters. The NIR-based algorithm also has the potential to further extend to the visible bands to derive the IOP properties, such as $a_{ph}(\lambda)$, $a_{cdom}(\lambda)$ over turbid coastal and inland waters.

In this paper, we further demonstrate that the NIR-based backscattering coefficients derived from the Visible Infrared Imaging Radiometer Suite (VIIRS) onboard the Suomi National Polar-orbiting Partnership (SNPP) can be used to accurately compute TSM concentrations due to the intrinsic

relationship between the sediment particle backscattering coefficients and the TSM concentration. For this purpose, we use in situ measurements of the TSM and $nL_w(\lambda)$ data in Lake Taihu to develop a set of the NIR-based TSM algorithms for VIIRS-SNPP applications in China's Lake Taihu. The accuracy of these algorithms is assessed using statistical analysis. Following the TSM algorithm development, VIIRS measurements from 2012 to 2016 are processed to derive $nL_w(\lambda)$ spectra using the SWIR-based atmospheric correction [39] with VIIRS SWIR M8 and M10 bands (1238 and 1601 nm). Particle backscattering coefficients at the two VIIRS NIR bands 745 and 862 nm, $b_{bp}(745)$ and $b_{bp}(862)$, are then calculated. We apply this set of the VIIRS TSM algorithms to derive TSM data over Lake Taihu in the VIIRS period. Furthermore, VIIRS-derived TSM data in Lake Taihu are validated using in situ TSM measurements in the VIIRS period. Finally, time series and seasonal variability of TSM concentrations in Lake Taihu are derived and analyzed.

2. Data and Method

2.1. China's Lake Taihu

Lake Taihu is located in the Yangtze River Delta (Figure 1) with an areal coverage of $\sim 2300 \text{ km}^2$ and a mean depth of $\sim 2 \text{ m}$. Waters in Lake Taihu are consistently turbid all year with winter and summer ranking the most and least turbid seasons in the lake [40–42]. In addition, Lake Taihu has frequent algal blooms in the spring-summer that pollute the lake water. MODIS-Aqua observations were used to monitor the development of the blue-green algae (*Microcystis*) in the spring of 2007 [40] that adversely affected the normal lives of several million residents. As the third-largest inland freshwater lake in China, Lake Taihu has experienced significant environmental issues in recent years [43]. Studies have shown that the 2007 drinking water crisis is linked to climate variability and lake management [44]. In addition to the TSM and turbidity in Lake Taihu, other environmental and water quality parameters, such as phytoplankton and algal blooms [45], lake eutrophication [46], Chl-a and primary production variations [47], and CDOM [48,49] have also been investigated.

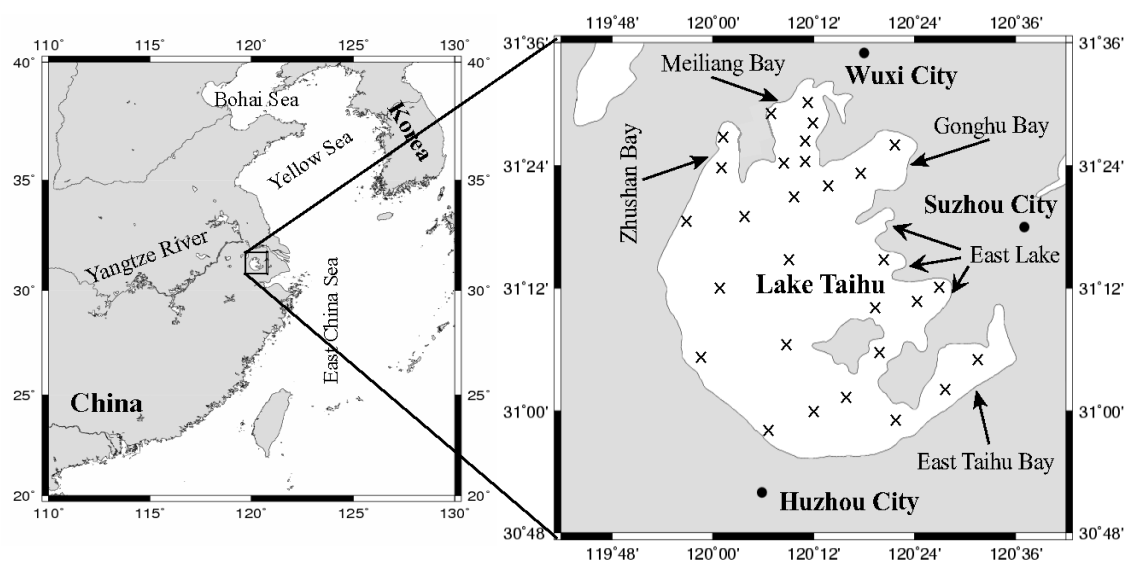


Figure 1. Maps of China's inland Lake Taihu. Locations of the in situ TSM measurements. Between 2012 and 2016 are marked as "x" in Lake Taihu.

It is noted that Lake Taihu is featured with high turbidity with the $K_d(490)$ values generally over $\sim 2 \text{ m}^{-1}$, and reaching $\sim 3\text{--}4 \text{ m}^{-1}$ in the winter and spring seasons for most part of the lake [40]. This shows that Lake Taihu is an optically-deep water body with negligible bottom effects on the satellite-measured $nL_w(\lambda)$ spectra. On the other hand, the water absorption is significantly larger at

the NIR wavelengths than that at visible wavelengths. This further suggests that the lake is optically deep and negligible bottom effects at the VIIRS NIR bands even though the bottom reflection might sometime exist for the visible bands in some regions, such as a small portion of the southeast Lake Taihu with shallower depths and low water turbidity.

2.2. In Situ Measurements of $nL_w(\lambda)$ and TSM Concentration

To develop the TSM algorithms for VIIRS observations, we used the in situ measurements of $nL_w(\lambda)$ and TSM concentrations between 2006 and 2007 in Lake Taihu. In that period, five cruises were carried out to collect optical measurements and water samples for biological and bio-optical properties. There were about 50 sample stations covering the entire area of Lake Taihu for each cruise. The time periods for the five cruises were 7–9 January 2006, 29 July–1 August 2006, 12–15 October 2006, 7–9 January 2007, and 25–27 April 2007. The optical and biogeochemical parameters from the in situ measurements at each station include hyperspectral remote sensing reflectance for wavelengths between 350 and 1050 nm and TSM concentration.

The optical measurements were made, and the water samples were collected, at a depth of 50 cm below the surface, comprising a total of 50 sites covering different regions of the lake. In order to obtain high-quality in situ remote sensing reflectance, measurements were carried out under clear sky conditions with no wind or very low winds during the hours of 8:30–16:30. At each sampling site, the spectra were measured 10 times to optimize the signal-to-noise ratio (SNR), and thus reduce the error of in situ measurements. Downwelling radiance and upwelling total radiance measurements were made with an ASD field spectrometer (Analytical Devices, Inc., Boulder, CO, USA) with a spectral response of 350 to 1050 nm, a spectral resolution of 3 nm, and a sampling interval of 1 nm. The water-leaving radiance $L_w(\lambda, 0^+)$ was derived after deducting the contribution of sky radiance $L_{sky}(\lambda)$. The remote sensing reflectance above the water surface $R_{rs}(\lambda)$ was calculated as the ratio of water-leaving upwelling radiance $L_w(\lambda, 0^+)$ to incident downwelling irradiance $E_d(\lambda, 0^+)$. The detailed protocols of the in situ data collection and processing can be found in [50,51].

In the VIIRS period between 2012 and 2016, frequent in situ measurements of TSM concentrations at a number of monitoring stations in Lake Taihu were taken. These monitoring stations were set up by the Nanjing Institute of Geography and Limnology, Chinese Academy of Sciences, aiming to monitor and assess long-term ecosystem changes in Lake Taihu. The TSM in situ measurements coincident with the VIIRS observations between 2012 and 2016 were used to validate the VIIRS-derived TSM retrievals.

2.3. VIIRS-SNPP Data and Ocean Color Data Processing

VIIRS-SNPP was launched on 28 October 2011. VIIRS has 22 spectral bands covering a spectral range from 0.410 to 12.013 μm , which include 14 reflective solar bands (RSBs), seven thermal emissive bands (TEBs), and a panchromatic day/night band (DNB) [52]. VIIRS has similar spectral bands as MODIS, which provide observations of Earth's atmosphere, land, and ocean properties [53]. One of the primary goals of the VIIRS mission is to provide data continuity from MODIS for the science and user community with Environmental Data Records (EDR) over global oceanic waters to enable assessment of climatic and environmental variability [54]. Ocean color EDR is a key product suite derived from VIIRS [55].

Specifically, VIIRS-SNPP has five visible bands (M1–M5) with nominal central wavelengths of 410, 443, 486, 551, and 671 nm, two NIR bands (M6 and M7) at wavelengths of 745 and 862 nm, and three SWIR bands (M8, M10, and M11) at wavelengths of 1238, 1601, and 2257 nm for satellite ocean color data processing. Note that VIIRS band wavelengths are indicated for the band nominal center wavelength. In addition, effective band center wavelengths can also be calculated for the VIIRS-SNPP in order to remove the sensor out-of-band (OOB) effects following the approach in Wang et al. [56]. On-orbit vicarious calibrations for VIIRS-SNPP were carefully carried out using the in situ $nL_w(\lambda)$ spectra from the Marine Optical Buoy (MOBY) [57] in waters off Hawaii and over the South Pacific Gyre (SPG) [58]. Similar to the standard NIR atmospheric correction algorithm [59,60] with two NIR

bands (745 and 862 nm for VIIRS), the SWIR-based atmospheric correction algorithm with VIIRS SWIR 1238 and 1601 nm bands has been used in deriving the $nL_w(\lambda)$ spectra [39]. The SWIR atmospheric correction algorithm is based on the fact that the waters are more strongly absorbing at the SWIR wavelengths than those at the NIR wavelengths [37]. Thus, normally-not-black turbid waters in the NIR bands can still be black for the SWIR bands [32,39]. Consequently, VIIRS measurements at the SWIR bands can be used to determine the aerosol type and estimate the atmospheric effects in the visible and NIR by extrapolating the aerosol effect from the SWIR wavelengths to visible and NIR wavelengths using appropriate aerosol models [39].

The Multi-Sensor Level-1 to Level-2 (MSL12), which is the official NOAA VIIRS ocean color data processing system, has been used for processing satellite ocean color data from Sensor Data Records (SDR) (or Level-1B) to ocean color EDR (or Level-2) products for VIIRS-SNPP. In recent years, MSL12 has made several important improvements and enhancements. In particular, these improvements and updates include the SWIR-based and NIR-SWIR combined atmospheric correction algorithms for improved ocean color data products in coastal and inland waters [39,61,62]. In this study, VIIRS-SNPP observations over Lake Taihu made between 2012 and 2016 were processed using the MSL12 ocean color data processing system to produce $nL_w(\lambda)$ at the visible and NIR bands. Several studies have shown that MSL12 can produce good quality $nL_w(\lambda)$ spectra in both open oceans and coastal regions from various satellite ocean color sensors, e.g., MODIS-Aqua, VIIRS-SNPP, and the Korean Geostationary Ocean Color Imager (GOCI) [26,40,55,62].

2.4. The NIR-IOP-Based TSM Algorithm

As a pre-requisite, $b_{bp}(\lambda)$ data at the NIR wavelengths are required in order to derive the TSM concentration. To calculate the $b_{bp}(\lambda)$, satellite-derived remote sensing reflectance $R_{rs}(\lambda)$ is converted to subsurface remote sensing reflectance $r_{rs}(\lambda)$ [63] by:

$$r_{rs}(\lambda) = \frac{R_{rs}(\lambda)}{(0.52 + 1.7R_{rs}(\lambda))} \quad (1)$$

Gordon et al. [28] have shown that subsurface remote sensing reflectance $r_{rs}(\lambda)$ can be computed quadratically with ocean IOPs based on the reflectance model, i.e.:

$$r_{rs}(\lambda) = g_1 \left(\frac{b_b(\lambda)}{(a(\lambda) + b_b(\lambda))} \right) + g_2 \left(\frac{b_b(\lambda)}{(a(\lambda) + b_b(\lambda))} \right)^2 \quad (2)$$

where $r_{rs}(\lambda)$ is the remote-sensing reflectance just beneath the water surface, and g_1 and g_2 are constant values of 0.0949 and 0.0794, respectively.

In comparison with $nL_w(\lambda)$ results in visible bands, which are usually used for IOP modeling, pure seawater absorption coefficients $a_w(\lambda)$ at the NIR bands are significantly larger than those of other seawater constituents [37], i.e., $a_w(\lambda) \gg a_{ph}(\lambda)$, $a_g(\lambda)$, and $a_d(\lambda)$ for the NIR bands. For example, $a_w(862)$ is $\sim 5 \text{ m}^{-1}$, compared with $a_{ph}(862)$, $a_g(862)$, and $a_d(862)$ which are close to 0 [64–67]. Therefore, with the spectral features of $a_w(\lambda)$, $a_{ph}(\lambda)$, $a_g(\lambda)$, and $a_d(\lambda)$ at the NIR wavelengths, $b_b(\lambda)/(a(\lambda) + b_b(\lambda))$ can be approximated as (at the NIR bands):

$$\left(\frac{b_b(\lambda)}{(a(\lambda) + b_b(\lambda))} \right) \approx \left(\frac{b_b(\lambda)}{(a_w(\lambda) + b_b(\lambda))} \right) \quad (3)$$

With this approximation, $b_b(745)$ and $b_b(862)$ can be easily computed from Equations (1)–(3) using VIIRS-derived $nL_w(745)$ and $nL_w(862)$. Consequently, $b_{bp}(745)$ and $b_{bp}(862)$ can be calculated after removing water backscattering coefficients $b_{bw}(745)$ and $b_{bw}(862)$, which are several orders smaller than $b_{bp}(745)$ and $b_{bp}(862)$ in the coastal and inland waters.

Using the in situ $nL_w(\lambda)$ at the corresponding VIIRS NIR bands at 745 and 862 nm, $b_{bp}(\lambda)$ values at the wavelengths of 551, 671, 745, and 862 nm were derived following the Shi and Wang [33,68]

approach. In brief, $b_{bp}(745)$ and $b_{bp}(862)$ are first derived using Equations (1)–(3) with the VIIRS-derived $nL_w(745)$ and $nL_w(862)$. Since $b_{bp}(\lambda)$ is spectrally correlated, and can be generally modeled as a function of $b_{bp}(\lambda)$ at a reference wavelength [65,69], the power law slope η can then be consequently computed with $b_{bp}(745)$ and $b_{bp}(862)$ [68]. With the derived power law slope η , $b_{bp}(\lambda)$ in the VIIRS visible bands, e.g., $b_{bp}(443)$, $b_{bp}(551)$, can be computed using the reference $b_{bp}(745)$ and the derived power law slope η .

Figure 2a–d show the scatter plots of in situ-derived $b_{bp}(\lambda)$ versus TSM for $b_{bp}(\lambda)$ at the wavelengths of 551, 671, 745, and 862 nm, respectively. A quasi-linear relationship between TSM and $b_{bp}(862)$ can be found (Figure 2d) for the entire TSM range. However, the relationship between TSM and $b_{bp}(\lambda)$ becomes nonlinear at shorter wavelengths (Figure 2a–c). Specifically, $b_{bp}(551)$ is much less sensitive to the TSM change for the TSM over ~ 100 mg/L (Figure 2a). This shows that the relationship between the TSM and $b_{bp}(\lambda)$ is wavelength-dependent, and a nonlinear function, as in Equation (4), is necessary to characterize the relationship between the TSM and $b_{bp}(\lambda)$, in particular, for $b_{bp}(\lambda)$ at the shorter visible wavelengths.

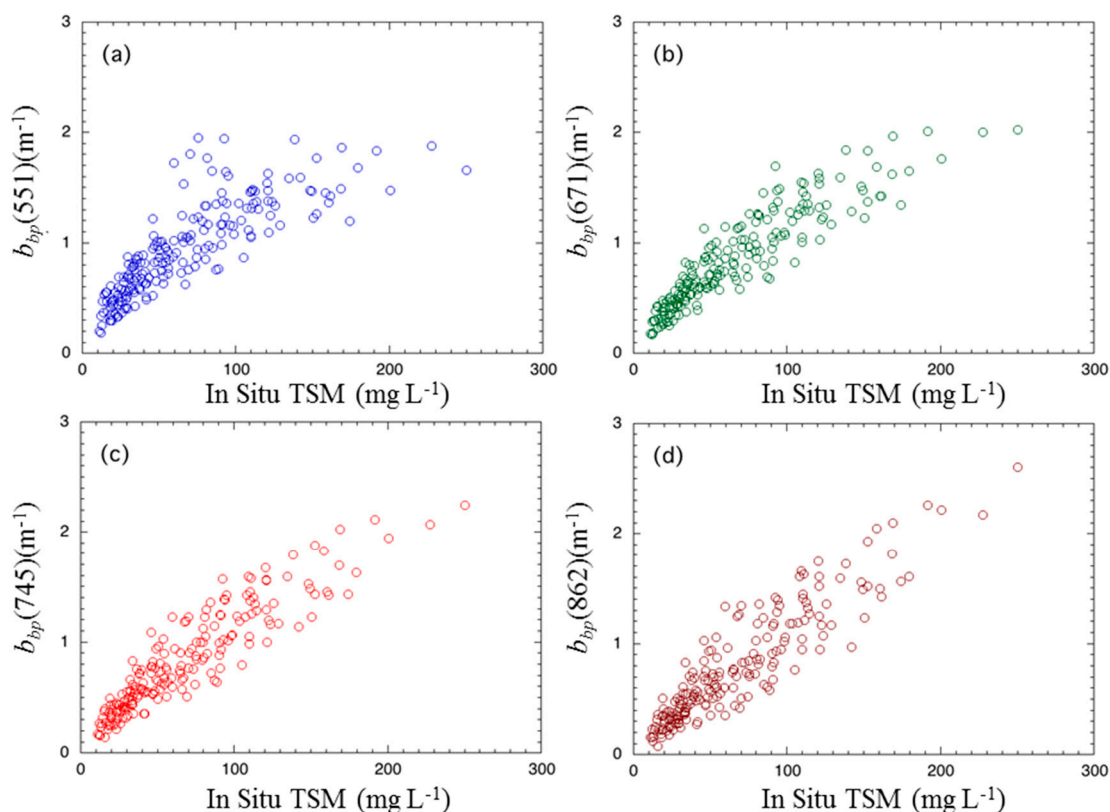


Figure 2. Scatter plots of in situ-derived $b_{bp}(\lambda)$ versus in situ TSM concentration in Lake Taihu for $b_{bp}(\lambda)$ at wavelengths of (a) 551 nm, (b) 671 nm, (c) 745 nm, and (d) 862 nm.

Consequently, the particle backscattering of the sediment in the water column, $b_{bp}(\lambda)$, can generally be related to the TSM concentration in a polynomial equation as:

$$b_{bp}(\lambda) = \sum_{i=1}^N m_i(\lambda) [TSM \times b_{bp}^*(\lambda)]^i \quad (4)$$

where $b_{bp}^*(\lambda)$ is the mass-specific particle backscattering coefficient, $m_i(\lambda)$ is the constant coefficient for each term, i is the degree of the polynomial, and TSM is the TSM concentration in the water column. In comparison to a simple linear equation, a nonlinear polynomial equation for the relationship of

$b_{bp}(\lambda)$ and TSM is able to provide more flexibility and generality for addressing the relationship of $b_{bp}(\lambda)$ and TSM in the turbid waters with a wide-range of TSM concentrations.

On the other hand, $b_{bp}^*(\lambda)$ is, in general, a constant value for a specific region since it is determined by the particle size distribution, particle shapes, and compositions. Consequently, Equation (4) shows that $b_{bp}(\lambda)$ is proportional to the TSM concentration. Conversely, TSM concentration can also be expressed as a nonlinear function of $b_{bp}(\lambda)$ in order to compute the TSM concentration from backscattering coefficients $b_{bp}(\lambda)$. In this study, we use a quadratic function ($N = 2$) to compute the TSM concentration from the backscattering coefficient $b_{bp}(\lambda)$ in the NIR wavelengths, i.e.:

$$TSM = n_1(\lambda)b_{bp}(\lambda) + n_2(\lambda)[b_{bp}(\lambda)]^2 \quad (5)$$

where $n_1(\lambda)$ and $n_2(\lambda)$ are coefficients to best fit TSM to $b_{bp}(\lambda)$ relationship in Equation (5). Note that Equation (5) assumes that $n_0(\lambda) = 0$, i.e., $TSM = 0$ for $b_{bp}(\lambda) = 0$.

Specifically, using Equations (1)–(3), the in situ $nL_w(\lambda)$ at the two NIR wavelengths can be first converted to in situ $b_b(745)$ and $b_b(862)$. Next, the in situ TSM algorithms can then be developed using the in situ $b_b(745)$ and $b_b(862)$ data and the corresponding TSM concentration. Finally, the same TSM algorithms developed using the in situ data for Lake Taihu can be used for VIIRS measurements.

Using $nL_w(\lambda)$ at the NIR bands derived from the SWIR-based atmospheric correction [39,61] with the MSL12 ocean color data processing system, we can first compute the satellite-derived $b_{bp}(745)$ and $b_{bp}(862)$ in Lake Taihu. Then TSM algorithms can be applied to the VIIRS-derived $b_{bp}(745)$ and $b_{bp}(862)$ to produce the VIIRS-derived TSM products in Lake Taihu. With the VIIRS-derived $b_{bp}(\lambda)$ and TSM products, we can produce the seasonal climatology and interannual variations of $b_{bp}(\lambda)$ and TSM in Lake Taihu from 2012 to 2016. The numbers of VIIRS granules to produce seasonal climatology data are more or less the same, thus, seasonal $b_{bp}(\lambda)$ and TSM can be compared with each other without artificial sampling biases. Similarly, the interannual variation of $b_{bp}(\lambda)$ and TSM in Lake Taihu is also computed on a season-by-season basis.

3. Results

3.1. VIIRS TSM Algorithm for Lake Taihu

Using the in situ $nL_w(\lambda)$ at the NIR 745 and 862 nm and the corresponding TSM concentrations collected in various experimental investigations in 2006 and 2007 before the VIIRS-SNPP launch, two TSM algorithms were developed in Equation (2) with the least-square fitting approach. The algorithm for deriving TSM concentration from $b_{bp}(745)$ is as follows:

$$TSM^{(745)} = 70.60b_{bp}(745) + 10.53[b_{bp}(745)]^2 \quad (6)$$

and the algorithm for deriving TSM concentration from $b_{bp}(862)$ is:

$$TSM^{(862)} = 91.61b_{bp}(862) - 5.31[b_{bp}(862)]^2 \quad (7)$$

Figure 3 shows the performance of the two TSM algorithms in comparison with the in situ TSM measurements. In general, data from both $TSM^{(745)}$ (Figure 3a) and $TSM^{(862)}$ (Figure 3b) match well with the in situ TSM measurements. The Pearson correlation coefficients R for $TSM^{(745)}$ -derived (Figure 3a) and $TSM^{(862)}$ -derived (Figure 3b) versus TSM-in situ data are 0.93 and 0.92, respectively. It is also noted that the relationship for both $TSM^{(745)}$ versus TSM-in situ and $TSM^{(862)}$ versus TSM-in situ works well for the entire TSM range in Lake Taihu. This demonstrates that both NIR- $b_{bp}(\lambda)$ -based algorithms work well for moderately- to highly-turbid waters. It also indicates that the approximation for the backscattering relationship shown in Equation (5) is indeed valid. Thus, $b_{bp}(745)$ and $b_{bp}(862)$ can be computed analytically in order to produce the TSM products in Lake Taihu.

Figure 3c shows the matchup results between the $TSM^{(745)}$ and $TSM^{(862)}$. Indeed, they are consistent with each other with negligible differences (as expected). The correlation between $TSM^{(745)}$ and $TSM^{(862)}$ reaches over 0.99, and suggests that both $TSM^{(745)}$ and $TSM^{(862)}$ can be applied to VIIRS-derived $nL_w(\lambda)$ and $b_{bp}(\lambda)$ at the NIR bands 745 and 862 nm to characterize and quantify the TSM variability in Lake Taihu.

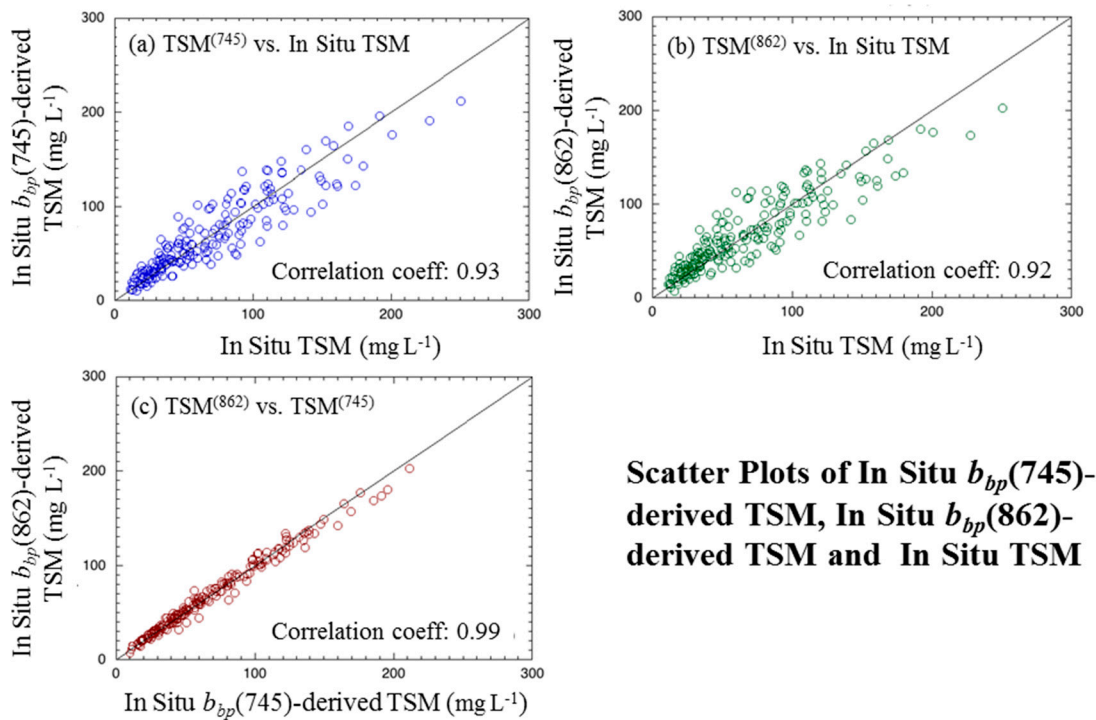


Figure 3. Scatter plots for (a) $b_{bp}(745)$ -derived versus in situ-measured TSM, (b) $b_{bp}(862)$ -derived versus in situ-measured TSM, and (c) $b_{bp}(862)$ -derived versus $b_{bp}(745)$ -derived TSM.

3.2. VIIRS TSM Algorithm Validation

In the VIIRS period between 2012 and 2016, there were a total of 126 good matches of VIIRS observations and in situ measurements, i.e., valid VIIRS TSM retrievals and in situ measurements at these stations on the same day. These matchup locations at the monitoring stations are located across Lake Taihu. Figure 1 shows the locations of these monitoring stations (marked with “×”). The in situ measurements were typically taken within ± 3 h of VIIRS overpassing Lake Taihu. Of the 126 matchups, there are 21, 58, 29, and 18 matchups in years 2012, 2013, 2015, and 2016, respectively. There were no matchups in 2014.

Figure 4a shows the scattering plot of VIIRS $TSM^{(745)}$ versus in situ TSM, and Figure 4b shows the scattering plot of VIIRS $TSM^{(862)}$ versus in situ TSM for all matchups acquired between 2012 and 2016. In general, both VIIRS-derived $TSM^{(745)}$ and $TSM^{(862)}$ compared well with in situ TSM data. In fact, the mean ratios of VIIRS-derived TSM and in situ TSM are 0.943 and 0.971 for $TSM^{(745)}$ and $TSM^{(862)}$, respectively, with corresponding standard deviation (STD) values of 0.186 and 0.198, respectively (Table 1). The Pearson correlation coefficients between the VIIRS-derived TSM and the in situ ones are 0.861 and 0.873, and normalized root mean square errors (NRMSEs) are 0.234 and 0.226 for $TSM^{(745)}$ and $TSM^{(862)}$, respectively, even though the time difference between the satellite overpass and the in situ TSM measurements could be up to several hours. In the logarithmic domain corresponding to Figure 4, the intercept and slope from the regression analysis are 0.208 and 0.908 for $TSM^{(745)}$ and 0.132 and 0.921 for $TSM^{(862)}$. With the validation of the accuracy of these two TSM algorithms for

VIIRS observations, the seasonal and interannual variability of the TSM in Lake Taihu from long-term satellite observations can be assessed with good accuracy.

Table 1. Statistics for VIIRS-derived and in situ-measured TSM comparison in Lake Taihu.

TSM Algorithm	Matchup Number	Mean Ratio	STD for Ratio	Correlation Coefficient	NRMSE
$TSM^{(745)}$	126	0.943	0.186	0.861	0.234
$TSM^{(862)}$	126	0.971	0.198	0.873	0.226

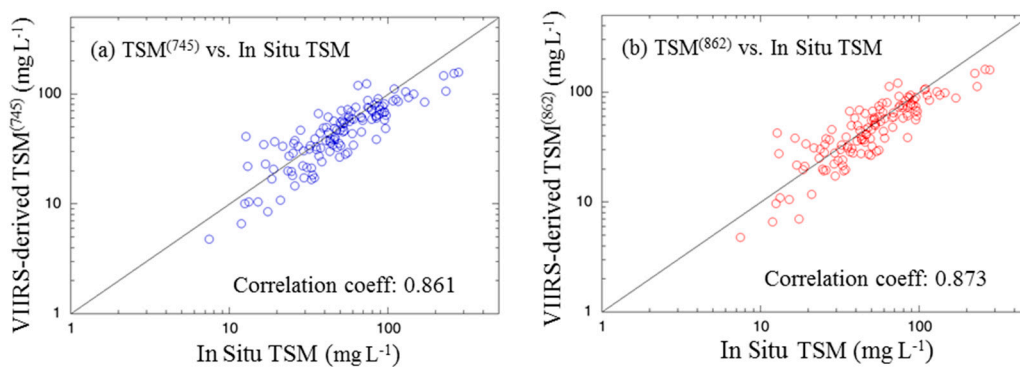


Figure 4. Scatter plots of (a) VIIRS $b_{bp}(745)$ -derived $TSM^{(745)}$ versus in situ-measured TSM and (b) VIIRS $b_{bp}(862)$ -derived $TSM^{(862)}$ versus in situ-measured TSM.

The validation of the two TSM algorithms also shows that both of the satellite TSM algorithms are valid for retrieving the VIIRS TSM products in Lake Taihu. This also further implies that the VIIRS-derived $nL_w(\lambda)$ spectra are reasonably accurate and reliable in Lake Taihu using the SWIR atmospheric correction algorithm. Otherwise, significant TSM retrieval bias and a high uncertainty in terms of the STD could occur since the TSM algorithms are developed with the in situ $nL_w(\lambda)$ measurements from Lake Taihu. It should be particularly noted that the in situ data used for developing the VIIRS TSM algorithms and those for algorithm validation were acquired at different times.

3.3. Seasonal Variability of the NIR-Based TSM in Lake Taihu

As demonstrated in Wang et al. [40,41] with MODIS water property products in Lake Taihu, Lake Taihu experienced significant spatial and temporal variations in terms of the water optical, biological, and biogeochemical properties. Using VIIRS-SNPP five-year observations from 2012 to 2016, seasonal climatology images of $nL_w(745)$ and $nL_w(862)$ were also derived. Figure 5 shows the seasonal climatology images of $nL_w(745)$ (Figure 5a–d) and $nL_w(862)$ (Figure 5e–h) for the season of boreal spring (March–May), summer (June–August), autumn (September–November), and winter (December–February). For each pixel, all of the corresponding valid $nL_w(\lambda)$ spectra derived from VIIRS observations for that season (i.e., spring, summer, fall, and winter) between 2012 and 2016 are selected, and the median value of the valid $nL_w(\lambda)$ at that pixel is calculated as the climatology $nL_w(\lambda)$ value for that season. Similarly, the seasonal climatology of $b_{bp}(\lambda)$ and $TSM(\lambda)$ is also computed. In general, $nL_w(745)$ and $nL_w(862)$ in Lake Taihu show significant seasonal variability with enhanced $nL_w(745)$ and $nL_w(862)$ in the winter season, and depressed $nL_w(745)$ and $nL_w(862)$ in the summer season. As an example, $nL_w(745)$ actually reaches over $\sim 3 \text{ mW cm}^{-2} \mu\text{m}^{-1} \text{ sr}^{-1}$ in the Southern Lake Taihu in the winter, while its value is only $\sim 1 \text{ mW cm}^{-2} \mu\text{m}^{-1} \text{ sr}^{-1}$ in the summer. However, in Meiliang Bay part of Northern Lake Taihu (see the location in Figure 1), $nL_w(745)$ peaks in the summer and autumn, while low $nL_w(745)$ is observed in the winter season.

The spatial variability of $nL_w(745)$ and $nL_w(862)$ in each season is also significant. In winter, $nL_w(745)$ and $nL_w(862)$ in the southern lake region are ~ 3 – 4 times larger than those in the Northern Lake Taihu. However, in summer the $nL_w(745)$ and $nL_w(862)$ are higher in Northern Lake Taihu than

in Southern Lake Taihu. It is also noted that both the temporal and spatial variations of VIIRS $nL_w(745)$ and $nL_w(862)$ are consistent with the $nL_w(859)$ and $K_d(490)$ derived from MODIS-Aqua observations in Lake Taihu [40,41].

We also derive VIIRS seasonal $b_{bp}(862)$ and $TSM^{(862)}$ from $nL_w(862)$ in Lake Taihu. Figure 6 shows $b_{bp}(862)$ (Figure 6a–d) and $TSM^{(862)}$ (Figure 6e–h) in the spring, summer, autumn, and winter seasons. As expected, similar results are obtained for $b_{bp}(745)$ and $TSM^{(745)}$ (not shown). Due to the intrinsic relationship between $b_{bp}(\lambda)$ and $nL_w(\lambda)$ in the NIR wavelengths, the spatial and seasonal changes of the $b_{bp}(745)$ and $b_{bp}(862)$ follow the changes of $nL_w(745)$ and $nL_w(862)$ as expected. Significantly higher $b_{bp}(862)$ and $TSM^{(862)}$ can be found in Southern Lake Taihu in winter (Figure 6d,h). In contrast, $b_{bp}(862)$ and $TSM^{(862)}$ are actually lower in Southern Lake Taihu than those in Northern Lake Taihu in the summer (Figure 6b,f). The peaks in $b_{bp}(862)$ and $TSM^{(862)}$ during the winter might be attributed to the enhanced sediment suspension due to strong monsoon winds [24].

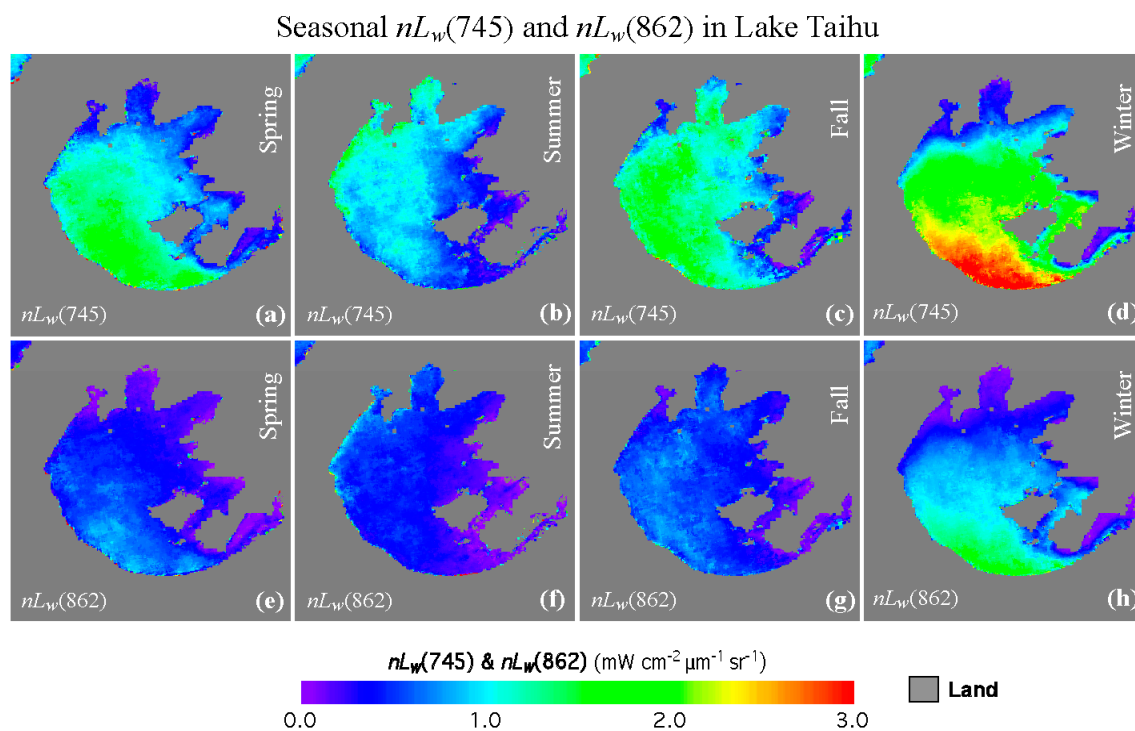


Figure 5. Seasonal climatology $nL_w(745)$ images (a–d) and $nL_w(862)$ images (e–h) for spring, summer, autumn, and winter from VIIRS 2012–2016 measurements, respectively.

The particle backscattering coefficient $b_{bp}(\lambda)$ is spectrally correlated and generally can be modeled as a function of $b_{bp}(\lambda)$ at another wavelength [65], i.e.,

$$b_{bp}(\lambda) = b_{bp}(\lambda_0) \left(\frac{\lambda_0}{\lambda} \right)^\eta \quad (8)$$

Examination of $b_{bp}(862)$ and $b_{bp}(745)$ (not shown here) shows that they are almost identical in terms of both spatial pattern and magnitude in the winter. This suggests that the value of power law slope, η , is close to 0. On the other hand, $b_{bp}(745)$ is higher than $b_{bp}(862)$ in the spring, summer, and autumn, suggesting that the value of power law slope, η , is positive. Since η is related to the suspended sediment properties, such as the particle size distribution, particle compositions, etc., the seasonal change of the power law slope, η , might have further biological and biogeochemical implications for Lake Taihu.

Using Equations (6) and (7), seasonal variability of TSM concentration in Lake Taihu is also derived. Figure 6 shows TSM concentration $TSM^{(862)}$ (Figure 6e–h) derived from $b_{bp}(862)$ in the four seasons. In the winter season, TSM concentration can reach over $\sim 100 \text{ mg L}^{-1}$ in Southern Lake Taihu, while low TSM concentration of $\sim 10 \text{ mg L}^{-1}$ is observed in Meiliang Bay, part of Northern Lake Taihu. Even though the formulae for $TSM^{(745)}$ and $TSM^{(862)}$ are different (Equations (6) and (7)), $TSM^{(862)}$ and $TSM^{(745)}$ (not shown here) are indeed similar for all four seasons in terms of the TSM values and their spatial patterns.

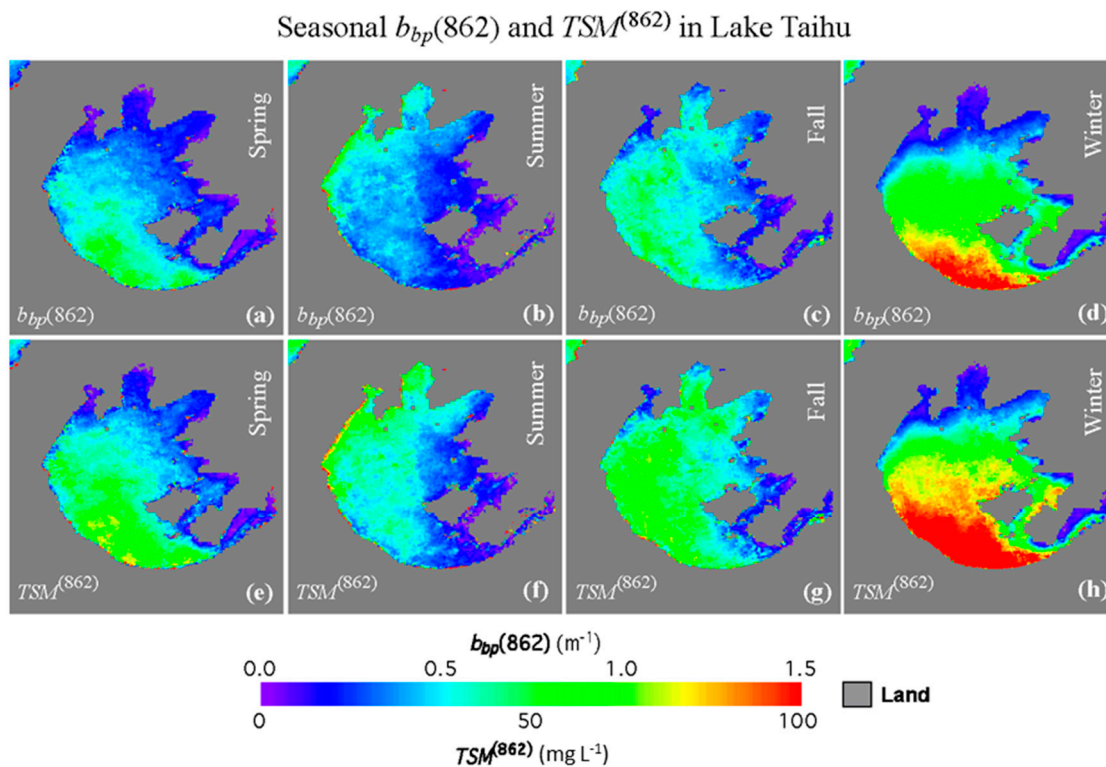


Figure 6. Seasonal climatology $b_{bp}(862)$ images (a–d) and $TSM^{(862)}$ images (e–h) for spring, summer, autumn, and winter from VIIRS 2012–2016 measurements, respectively.

It is also noted that the seasonal variation of $b_{bp}(\lambda)$ and TSM in Meiliang Bay is different from the other regions with pronounced $b_{bp}(\lambda)$ and TSM in summer, and autumn seasons (Figure 6), while peaks of $b_{bp}(\lambda)$ and TSM occurred in the winter season for the other parts of the lake. This might be attributed to the frequent occurrence of floating blue algae blooms in the three seasons in Meiliang Bay, which can consequently enhance the $nL_w(745)$ and $nL_w(862)$, and lead to possible overestimation of the TSM concentrations in the bay.

3.4. Interannual Variability of VIIRS NIR-Based Products in Lake Taihu

Previous studies show that the interannual variability of environmental parameters, such as Chl-a, $K_d(490)$, and primary production in Lake Taihu can be significant [40,47]. Figure 7 shows the composite images of $b_{bp}(862)$ from 2012 to 2016. Even though those spatial patterns of $b_{bp}(862)$ between 2012 and 2016 are similar to each other, interannual variability of the $b_{bp}(862)$ is also remarkable. In Meiliang Bay and Gonghu Bay, low $b_{bp}(862)$ were observed in 2014 and 2015 in comparison with the other years. In 2014 and 2015, the mean $b_{bp}(862)$ in Meiliang Bay was about 0.3 m^{-1} , while it reached over $\sim 0.4 \text{ m}^{-1}$ in the other years. Figure 7f–j show the corresponding $TSM^{(862)}$ in 2012–2016. In general, the spatial distributions of $TSM^{(862)}$ are similar to the spatial patterns of $b_{bp}(862)$ in each year. Enhanced $TSM^{(862)}$ over 100 mg/L was observed in southern Lake Taihu in the composite image of $TSM^{(862)}$ in 2014.

In terms of $TSM^{(862)}$ for the entire Lake Taihu, 2014 was the least turbid year. In addition to $b_{bp}(862)$ and $TSM^{(862)}$ between 2012 and 2016, $b_{bp}(745)$ and $TSM^{(745)}$ (not shown here) show similar results as $b_{bp}(862)$ and $TSM^{(862)}$ in these years.

Figure 8 shows the interannual variability of the $b_{bp}(\lambda)$ and TSM concentration for the entire Lake Taihu (Figure 8a,b). For the all of Lake Taihu, the average TSM concentration between 2012 and 2016 is $\sim 41 \text{ mg L}^{-1}$ with TSM ranging between $\sim 20\text{--}30 \text{ mg L}^{-1}$ in the summer and $\sim 60\text{--}80 \text{ mg L}^{-1}$ in the winter, respectively. Highest $b_{bp}(\lambda)$ and TSM concentrations occurred in the 2015–2016 winter with $b_{bp}(\lambda)$ reaching over $\sim 1.0 \text{ m}^{-1}$ and TSM concentrations over $\sim 80 \text{ mg L}^{-1}$. $TSM^{(745)}$ and $TSM^{(862)}$ are indeed close to each other between 2012 and 2016. This further suggests that both TSM algorithms can be used to quantitatively evaluate the long-term TSM variations in Lake Taihu.

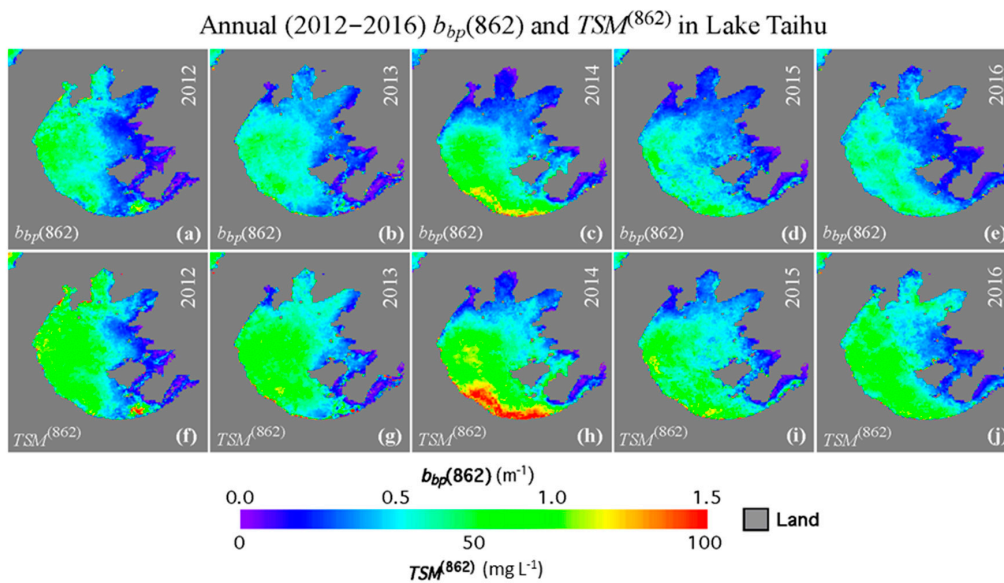


Figure 7. VIIRS-derived yearly composite images of $b_{bp}(862)$ (a–e) and $TSM^{(862)}$ (f–j) in the corresponding years of 2012–2016.

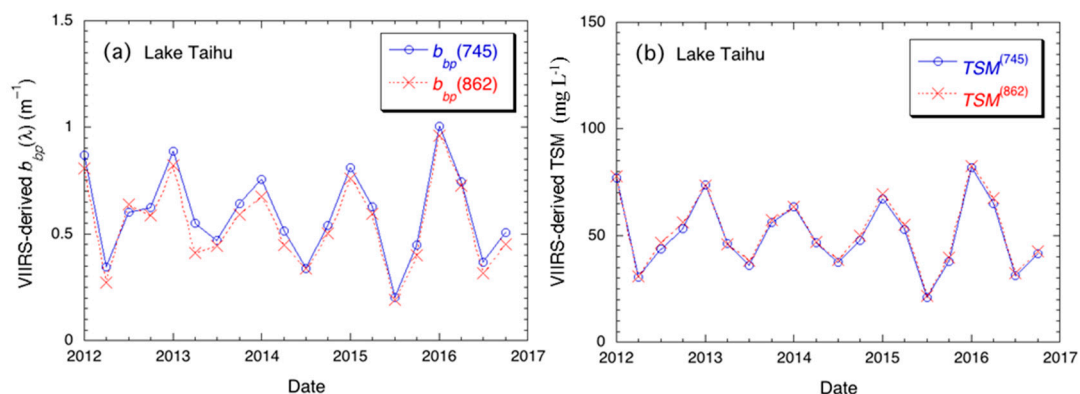


Figure 8. Variations of VIIRS-derived (a) $b_{bp}(745)$ and $b_{bp}(862)$, (b) $TSM^{(745)}$ and $TSM^{(862)}$ for the entirety of Lake Taihu.

It is also noted that the $TSM^{(745)}$ and $TSM^{(862)}$ algorithms are both developed from the in situ TSM concentration, $nL_w(745)$, and $nL_w(862)$. Negligible differences between the $TSM^{(745)}$ and $TSM^{(862)}$ algorithms provides further evidence that VIIRS $nL_w(745)$ and $nL_w(862)$ derived using the SWIR-based atmospheric correction algorithm in Lake Taihu are reasonably accurate and comparable to the in-situ $nL_w(\lambda)$ measurements. In combination with the negligible difference between $TSM^{(745)}$ and $TSM^{(862)}$,

it is also shown that both $TSM^{(745)}$ and $TSM^{(862)}$ can be confidently used to monitor, characterize, and quantify the TSM variation in Lake Taihu.

4. Discussion

In a recent study [33], we have shown that for highly turbid waters $b_{bp}(\lambda)$ in the NIR wavelengths can be derived analytically due to strong water absorption in the NIR wavelengths. In fact, $b_{bp}(\lambda)$ in visible wavelengths can also be derived with $b_{bp}(\lambda)$ in the NIR wavelengths. Using the International Ocean Color Coordinating Group (IOCCG) IOP dataset [65], it has been shown that this approach can derive accurate backscattering coefficients $b_{bp}(\lambda)$ in the visible and NIR wavelengths. Since there are no simultaneous $b_{bp}(\lambda)$ measurements in the in situ dataset in this study, the accuracy of $b_{bp}(745)$ and $b_{bp}(862)$ derived from in situ $nL_w(745)$ and $nL_w(862)$ cannot be evaluated directly. Examination of the in situ $a_{ph}(\lambda)$ and $a_{cdom}(\lambda)$ confirms that $a_w(\lambda)$ values at VIIRS 745 and 862 nm bands are generally two orders higher than the in situ $a_{ph}(\lambda)$ and $a_{cdom}(\lambda)$ in these two NIR bands. This provides evidence that the analytical Equations (1)–(5) are valid in turbid waters, such as Lake Taihu for deriving reasonable $b_{bp}(745)$ and $b_{bp}(862)$ values from VIIRS-measured $nL_w(745)$ and $nL_w(862)$.

In this study, we demonstrated that $b_{bp}(745)$ and $b_{bp}(862)$ can be used to compute TSM concentrations in Lake Taihu with good accuracy. Using the coincident in situ TSM measurements and VIIRS-derived $TSM^{(745)}$ and $TSM^{(862)}$, we further validate the VIIRS TSM retrieval algorithms in Lake Taihu. Previous studies have already shown that the SWIR-based atmospheric correction with MODIS can be used to drive $nL_w(\lambda)$ spectra with good accuracy in Lake Taihu [40,41], and the VIIRS sensor is well characterized and calibrated for all of the bands from the visible to SWIR wavelengths [55,70]. This shows that VIIRS-derived $nL_w(\lambda)$ spectra in Lake Taihu are reasonably accurate and can be used to produce other biogeochemical products, such as the TSM concentration. Similar approaches and procedures can be applied to develop the TSM algorithm for other sensors, such as MODIS-Aqua and other coastal and inland waters, if the in situ optical and TSM measurements are available. On the other hand, $b_{bp}(745)$ and $b_{bp}(862)$ in Lake Taihu can be related to TSM, which are eventually associated with the TSM bio-physical properties such as particle composition, mineral type, particle size distributions, etc., in addition to TSM concentration. Since these properties are stable over time in Lake Taihu, the TSM algorithms in Equations (6) and (7) can be safely applied to VIIRS observations to monitor, characterize, and quantify TSM variability in Lake Taihu.

In addition to developing a regional TSM algorithm for Lake Taihu, the main purpose of this study is to demonstrate the usefulness of the NIR IOP $b_{bp}(745)$ and $b_{bp}(862)$ for developing algorithms for other biological and biogeochemical products over turbid coastal and inland waters. The intrinsic relationships between $nL_w(\lambda)$ or $b_{bp}(\lambda)$ in the NIR wavelengths and TSM concentration imply that the formula for TSM as shown in Equations (6) and (7) for Lake Taihu should be reasonably accurate if $nL_w(\lambda)$ spectral shapes in the NIR wavelengths in other coastal and inland waters are similar to those in Lake Taihu. In fact, Shi and Wang (2014) [33] examined the ocean reflectance spectra in different regions in the Bohai Sea, Yellow Sea, and East China Sea from MODIS-Aqua observations. The NIR $nL_w(748)$ and $nL_w(869)$ show similar relationships for the Lake Taihu, Hangzhou Bay, and Yangtze River Estuary. The scatter plots of $nL_w(748)$ and $nL_w(869)$ in Lake Taihu, Hangzhou Bay, and Yangtze River Estuary generally overlap with each other in the range of $0\text{--}4 \text{ mW cm}^{-2} \mu\text{m}^{-1} \text{ sr}^{-1}$ for $nL_w(748)$, and the slopes of $nL_w(748)/nL_w(869)$ are similar in these three regions. In comparison, the spectral shapes in these three regions are virtually different from those in the Yellow River Estuary and the Subei Shoal. In fact, waters of these three regions have the same sediment source from the Yangtze River [71]. This indicates that the TSM algorithms from this study can also be applied across these regions. From a broad global perspective, these two NIR-based TSM algorithms can be applied to regions where VIIRS $nL_w(745)$ and $nL_w(862)$ have a similar relationship to that in Lake Taihu in order to derive reasonably good TSM products.

Even though other efforts exist to derive the TSM concentrations from satellite observations in the region [21,23,72], there are some limitations in these algorithms in comparison with the NIR-based

TSM algorithm. Particularly, $nL_w(\lambda)$ at the green and red bands can become saturated in highly-turbid waters [24,33]. Thus, for highly-turbid waters, $nL_w(\lambda)$ in the green and red wavelengths are not sensitive to the changes in the TSM concentrations. This suggests that the TSM algorithms based on $nL_w(\lambda)$ in green and red bands have physical and optical limitations in deriving accurate TSM concentration in highly turbid waters. In comparison, the NIR-based algorithm is valid over a wide range of TSM concentrations and necessary for highly-turbid waters. It is also noted that these two TSM algorithms do not have limitations for high TSM situations. Unlike the $nL_w(\lambda)$ in visible, $nL_w(\lambda)$ at these two NIR bands cannot become saturated in any season in Lake Taihu. However, caution should be given for applying these two algorithms to clear open ocean waters due to the accuracy of the satellite-derived $nL_w(\lambda)$ at NIR wavelengths. Particularly, the NIR $nL_w(\lambda)$ over the global open ocean is usually negligible. Even though Equation (5) shows that TSM concentration computation from Equations (1)–(3) can be calculated without any bias at low TSM levels, uncertainty in satellite-derived NIR $nL_w(\lambda)$ over the open ocean due to imperfect atmospheric correction can lead to errors in the retrieved TSM concentration.

5. Conclusions

In summary, we have demonstrated that TSM concentrations can be derived from the NIR-based $nL_w(\lambda)$ in Lake Taihu from VIIRS measurements. Using TSM data derived from VIIRS observations, seasonal and interannual variability of the TSM concentration in Lake Taihu has been characterized and quantified. In comparison with other TSM algorithms, the approach reported here uses the TSM and the NIR IOP (i.e., $b_{bp}(\lambda)$) relationship. Through the NIR $b_{bp}(\lambda)$ relationship, the TSM formulation can be expressed more clearly, in particular, how TSM should be related to water optics measurements. The NIR IOP-based TSM algorithm for turbid waters is more accurate, in particular, for waters with large TSM values, i.e., highly-turbid waters. From the global perspective, the IOP-based TSM algorithm has the potential to compute TSM concentration with good accuracy in the waters with similar NIR $nL_w(\lambda)$ spectral shapes as those in Lake Taihu. Indeed, for highly-turbid coastal and inland waters, accurate TSM data can only be derived using satellite-measured optical information at the NIR wavelengths.

Acknowledgments: This work was supported by the Joint Polar Satellite System (JPSS) funding and NOAA Product Development, Readiness, and Application (PDRA)/Ocean Remote Sensing (ORS) Program funding. The collection of in situ data in Lake Taihu (Y. Zhang) was supported by the National Natural Science Foundation of China (project nos. 41325001 and 41621002). We thank two anonymous reviewers for their useful comments. The views, opinions, and findings contained in this paper are those of the authors and should not be construed as an official NOAA or U.S. Government position, policy, or decision.

Author Contributions: Wei Shi carried out the main research work for developing algorithm, obtaining the results, and analyzing the data. Yunlin Zhang provided the in situ measurements, and help validate the TSM algorithm. Menghua Wang suggested for the topic, and contributed to the algorithm development and evaluation.

Conflicts of Interest: The authors declare no conflict of interest.

References

1. Wang, M.; Son, S.; Harding, L.W., Jr. Retrieval of diffuse attenuation coefficient in the Chesapeake Bay and turbid ocean regions for satellite ocean color applications. *J. Geophys. Res.* **2009**, *114*. [[CrossRef](#)]
2. Lee, Z.P.; Du, K.; Arnone, R. A model for the diffuse attenuation coefficient of downwelling irradiance. *J. Geophys. Res.* **2005**, *110*. [[CrossRef](#)]
3. Morel, A.; Huot, Y.; Gentili, B.; Werdell, P.J.; Hooker, S.B.; Franz, B.A. Examining the consistency of products derived from various ocean color sensors in open ocean (Case 1) waters in the perspective of a multi-sensor approach. *Remote Sens. Environ.* **2007**, *111*, 69–88. [[CrossRef](#)]
4. O'Reilly, J.E.; Maritorena, S.; Mitchell, B.G.; Siegel, D.A.; Carder, K.L.; Garver, S.A.; Kahru, M.; McClain, C.R. Ocean color chlorophyll algorithms for SeaWiFS. *J. Geophys. Res.* **1998**, *103*, 24937–24953. [[CrossRef](#)]
5. Hu, C.; Lee, Z.; Franz, B.A. Chlorophyll a algorithms for oligotrophic oceans: A novel approach based on three-band reflectance difference. *J. Geophys. Res.* **2012**, *117*. [[CrossRef](#)]

6. Wang, M.; Son, S. VIIRS-derived chlorophyll-a using the ocean color index method. *Remote Sens. Environ.* **2016**, *182*, 141–149. [[CrossRef](#)]
7. Behrenfeld, M.J.; Falkowski, P.G. Photosynthetic rates derived from satellite-based chlorophyll concentration. *Limnol. Oceanogr.* **1997**, *42*, 1–20. [[CrossRef](#)]
8. Antoine, D.; Morel, A. Oceanic primary production 1. Adaptation of a spectral light photosynthesis model in view of application to satellite chlorophyll observations. *Glob. Biogeochem. Cycles* **1996**, *10*, 43–55. [[CrossRef](#)]
9. Shi, W.; Wang, M. Satellite observations of flood-driven Mississippi River plume in the spring of 2008. *Geophys. Res. Lett.* **2009**, *36*. [[CrossRef](#)]
10. Mulder, T.; Syvitski, J.P.M. Turbidity currents generated at river mouths during exceptional discharges to the world oceans. *J. Geol.* **1995**, *103*, 285–299. [[CrossRef](#)]
11. Harden, C.P. Land use, soil erosion, and reservoir sedimentation in an Andean Drainage Basin in Ecuador. *Mountain Res. Dev.* **1993**, *13*, 177–184. [[CrossRef](#)]
12. Hu, C.; Muller-Karger, F.E. Response of sea surface properties to Hurricane Dennis in the eastern Gulf of Mexico. *Geophys. Res. Lett.* **2007**, *34*. [[CrossRef](#)]
13. Shi, W.; Wang, M. Observations of a Hurricane Katrina-induced phytoplankton bloom in the Gulf of Mexico. *Geophys. Res. Lett.* **2007**, *34*. [[CrossRef](#)]
14. Shi, W.; Wang, M. Three-dimensional observations from MODIS and CALIPSO for ocean responses to cyclone Nargis in the Gulf of Martaban. *Geophys. Res. Lett.* **2008**, *35*. [[CrossRef](#)]
15. Shi, W.; Wang, M.; Jiang, L. Spring-neap tidal effects on satellite ocean color observations in the Bohai Sea, Yellow Sea, and East China Sea. *J. Geophys. Res.* **2011**, *116*. [[CrossRef](#)]
16. Shi, W.; Wang, M.; Jiang, L. Tidal effects on ecosystem variability in the Chesapeake Bay from MODIS-Aqua. *Remote Sens. Environ.* **2013**, *138*, 65–76. [[CrossRef](#)]
17. Miller, R.L.; McKee, B. Using MODIS Terra 250 m imagery to map concentrations of total suspended matter in coastal waters. *Remote Sens. Environ.* **2004**, *93*, 259–266. [[CrossRef](#)]
18. Doxaran, D.; Froidefond, J.M.; Lavender, S.; Castaing, P. Spectral signature of highly turbid waters—Application with SPOT data to quantify suspended particulate matter concentrations. *Remote Sens. Environ.* **2002**, *81*, 149–161. [[CrossRef](#)]
19. Son, S.; Wang, M. Water properties in Chesapeake Bay from MODIS-Aqua measurements. *Remote Sens. Environ.* **2012**, *123*, 163–174. [[CrossRef](#)]
20. Tassan, S. An improved in-water algorithm for the determination of chlorophyll and suspended sediment concentration from Thematic Mapper data in coastal waters. *Int. J. Remote Sens.* **1993**, *14*, 1221–1229. [[CrossRef](#)]
21. Zhang, M.; Tang, J.; Dong, Q.; Song, Q.; Ding, J. Retrieval of total suspended matter concentration in the Yellow and East China Seas from MODIS imagery. *Remote Sens. Environ.* **2010**, *114*, 392–403. [[CrossRef](#)]
22. Mao, Z.H.; Chen, J.Y.; Pan, D.L.; Tao, B.Y.; Zhu, Q.K. A regional remote sensing algorithm for total suspended matter in the East China Sea. *Remote Sens. Environ.* **2012**, *124*, 819–831. [[CrossRef](#)]
23. Chen, J.; Quan, W.T.; Cui, T.W.; Song, Q.J. Estimation of total suspended matter concentration from MODIS data using a neural network model in the China eastern coastal zone. *Estuar. Coast. Shelf Sci.* **2015**, *155*, 104–113. [[CrossRef](#)]
24. Shi, W.; Wang, M. Satellite views of the Bohai Sea, Yellow Sea, and East China Sea. *Prog. Oceanogr.* **2012**, *104*, 30–45. [[CrossRef](#)]
25. Wang, M.; Shi, W. Estimation of ocean contribution at the MODIS near-infrared wavelengths along the east coast of the US: Two case studies. *Geophys. Res. Lett.* **2005**, *32*. [[CrossRef](#)]
26. Wang, M.; Tang, J.; Shi, W. MODIS-derived ocean color products along the China east coastal region. *Geophys. Res. Lett.* **2007**, *34*. [[CrossRef](#)]
27. Gitelson, A.A.; Schalles, J.F.; Hladik, C.M. Remote chlorophyll-a retrieval in turbid, productive estuaries: Chesapeake Bay case study. *Remote Sens. Environ.* **2007**, *109*, 464–472. [[CrossRef](#)]
28. Gordon, H.R.; Brown, O.B.; Evans, R.H.; Brown, J.W.; Smith, R.C.; Baker, K.S.; Clark, D.K. A Semianalytic Radiance Model of Ocean Color. *J. Geophys. Res. Atmos* **1988**, *93*, 10909–10924. [[CrossRef](#)]
29. Garver, S.A.; Siegel, D.A. Inherent optical property inversion of ocean color spectra and its biogeochemical interpretation: 1. Time series from the Sargasso Sea. *J. Geophys. Res.* **1997**, *102*, 18607–18625. [[CrossRef](#)]
30. Lee, Z.P.; Carder, K.L.; Arnone, R.A. Deriving inherent optical properties from water color: A multiple quasi-analytical algorithm for optically deep waters. *Appl. Opt.* **2002**, *41*, 5755–5772. [[CrossRef](#)] [[PubMed](#)]

31. Werdell, P.J.; Franz, B.A.; Bailey, S.W.; Feldman, G.C.; Boss, E.; Brando, V.E.; Dowell, M.; Hirata, T.; Lavender, S.J.; Lee, Z.P.; et al. Generalized ocean color inversion model for retrieving marine inherent optical properties. *Appl. Opt.* **2013**, *52*, 2019–2037. [[CrossRef](#)] [[PubMed](#)]
32. Shi, W.; Wang, M. An assessment of the black ocean pixel assumption for MODIS SWIR bands. *Remote Sens. Environ.* **2009**, *113*, 1587–1597. [[CrossRef](#)]
33. Shi, W.; Wang, M. Ocean reflectance spectra at the red, near-infrared, and shortwave infrared from highly turbid waters: A study in the Bohai Sea, Yellow Sea, and East China Sea. *Limnol. Oceanogr.* **2014**, *59*, 427–444. [[CrossRef](#)]
34. Le, C.F.; Li, Y.M.; Zha, Y.; Sun, D.Y.; Yin, B. Validation of a Quasi-Analytical Algorithm for highly turbid eutrophic water of Meiliang Bay in Taihu Lake, China. *IEEE Trans. Geosci. Remote Sens.* **2009**, *47*, 2492–2500.
35. Huang, J.; Chen, L.Q.; Chen, X.L.; Tian, L.Q.; Feng, L.; Yesou, H.; Li, F.F. Modification and validation of a quasi-analytical algorithm for inherent optical properties in the turbid waters of Poyang Lake, China. *J. Appl. Remote Sens.* **2014**, *8*. [[CrossRef](#)]
36. Qing, S.; Tang, J.W.; Cui, T.W.; Zhang, J. Retrieval of inherent optical properties of the Yellow Sea and East China Sea using a quasi-analytical algorithm. *Chin. J. Oceanol. Limn.* **2011**, *29*, 33–45. [[CrossRef](#)]
37. Hale, G.M.; Querry, M.R. Optical constants of water in the 200 nm to 200 μ m wavelength region. *Appl. Opt.* **1973**, *12*, 555–563. [[CrossRef](#)] [[PubMed](#)]
38. Kou, L.; Labrie, D.; Chylek, P. Refractive indices of water and ice in the 0.65–2.5 μ m spectral range. *Appl. Opt.* **1993**, *32*, 3531–3540. [[CrossRef](#)] [[PubMed](#)]
39. Wang, M. Remote sensing of the ocean contributions from ultraviolet to near-infrared using the shortwave infrared bands: Simulations. *Appl. Opt.* **2007**, *46*, 1535–1547. [[CrossRef](#)] [[PubMed](#)]
40. Wang, M.; Shi, W.; Tang, J.W. Water property monitoring and assessment for China's inland Lake Taihu from MODIS-Aqua measurements. *Remote Sens. Environ.* **2011**, *115*, 841–854. [[CrossRef](#)]
41. Wang, M.; Son, S.; Zhang, Y.; Shi, W. Remote sensing of water optical property for China's inland Lake Taihu using the SWIR atmospheric correction with 1640 and 2130 nm bands. *IEEE J. Sel. Top. Appl. Earth Obs. Remote Sens.* **2013**, *6*, 2505–2516. [[CrossRef](#)]
42. Shi, K.; Zhang, Y.L.; Zhu, G.W.; Liu, X.H.; Zhou, Y.Q.; Xu, H.; Qin, B.Q.; Liu, G.; Li, Y.M. Long-term remote monitoring of total suspended matter concentration in Lake Taihu using 250 m MODIS-Aqua data. *Remote Sens. Environ.* **2015**, *164*, 43–56. [[CrossRef](#)]
43. Qin, B.; Xu, P.; Wu, Q.; Luo, L.; Zhang, Y. Environmental issues of Lake Taihu, China. *Hydrobiologia* **2007**, *581*, 3–14. [[CrossRef](#)]
44. Qin, B.; Zhu, G.; Gao, G.; Zhang, Y.; Li, W.; Paerl, H.W.; Carmichael, W.W. A drinking water crisis in Lake Taihu, China: Linkage to climatic variability and lake management. *Environ. Manag.* **2010**, *45*, 105–112. [[CrossRef](#)] [[PubMed](#)]
45. Zhu, M.; Zhu, G.; Zhao, L.; Yao, X.; Zhang, Y.; Gao, G.; Qin, B. Influence of algal bloom degradation on nutrient release at the sediment-water interface in Lake Taihu, China. *Environ. Sci. Pollut. Res.* **2013**, *20*, 1803–1811. [[CrossRef](#)] [[PubMed](#)]
46. Qin, B.; Gao, G.; Zhu, G.; Zhang, Y.; Song, Y.; Tang, X.; Xu, H.; Deng, J. Lake eutrophication and its ecosystem response. *Chin. Sci. Bull.* **2013**, *58*, 961–970. [[CrossRef](#)]
47. Zhang, Y.; Qin, B.; Liu, M. Temporal-spatial variations of chlorophyll a and primary production in Meiliang Bay, Lake Taihu, China. *J. Plankton Res.* **2007**, *29*, 707–719. [[CrossRef](#)]
48. Yao, X.; Zhang, Y.L.; Zhu, G.W.; Qin, B.Q.; Feng, L.Q.; Cai, L.L.; Gao, G.A. Resolving the variability of CDOM fluorescence to differentiate the sources and fate of DOM in Lake Taihu and its tributaries. *Chemosphere* **2011**, *82*, 145–155. [[CrossRef](#)] [[PubMed](#)]
49. Zhang, Y.L.; van Dijk, M.A.; Liu, M.L.; Zhu, G.W.; Qin, B.Q. The contribution of phytoplankton degradation to chromophoric dissolved organic matter (CDOM) in eutrophic shallow lakes: Field and experimental evidence. *Water Res.* **2009**, *43*, 4685–4697. [[CrossRef](#)] [[PubMed](#)]
50. Zhang, Y.; Feng, L.; Li, J.; Luo, L.; Yin, Y.; Liu, M.; Li, Y. Seasonal-spatial variation and remote sensing of phytoplankton absorption in Lake Taihu, a large eutrophic and shallow lake in China. *J. Plankton Res.* **2010**, *32*, 1023–1037. [[CrossRef](#)]
51. Zhang, Y.; Liu, X.; Yin, Y.; Zhang, M.; Qin, B. A simple optical model to estimate diffuse attenuation coefficient of photosynthetically active radiation in an extremely turbid lake from surface reflectance. *Opt. Express* **2012**, *20*, 20482–20493. [[CrossRef](#)] [[PubMed](#)]

52. Shi, W.; Wang, M. Ocean dynamics observed by VIIRS day/night band satellite observations. *Remote Sens.* **2018**, *10*, 76. [[CrossRef](#)]
53. Goldberg, M.D.; Kilcoyne, H.; Cikanek, H.; Mehta, A. Joint Polar Satellite System: The United States next generation civilian polar-orbiting environmental satellite system. *J. Geophys. Res. Atmos.* **2013**, *118*, 13463–13475. [[CrossRef](#)]
54. McClain, C.R. A decade of satellite ocean color observations. *Ann. Rev. Mar. Sci.* **2009**, *1*, 19–42. [[CrossRef](#)] [[PubMed](#)]
55. Wang, M.; Liu, X.; Tan, L.; Jiang, L.; Son, S.; Shi, W.; Rausch, K.; Voss, K. Impact of VIIRS SDR performance on ocean color products. *J. Geophys. Res. Atmos.* **2013**, *118*, 10347–10360. [[CrossRef](#)]
56. Wang, M.; Naik, P.; Son, S. Out-of-band effects of satellite ocean color sensors. *Appl. Opt.* **2016**, *55*, 2312–2323. [[CrossRef](#)] [[PubMed](#)]
57. Clark, D.K.; Gordon, H.R.; Voss, K.J.; Ge, Y.; Broenkow, W.; Trees, C. Validation of atmospheric correction over the ocean. *J. Geophys. Res.* **1997**, *102*, 17209–17217. [[CrossRef](#)]
58. Wang, M.; Shi, W.; Jiang, L.; Voss, K. NIR- and SWIR-based on-orbit vicarious calibrations for satellite ocean color sensors. *Opt. Express* **2016**, *24*, 20437–20453. [[CrossRef](#)] [[PubMed](#)]
59. International Ocean-Colour Coordinating Group (IOCCG). *Atmospheric Correction for Remotely-Sensed Ocean-Colour Products*; Wang, M., Ed.; Reports of International Ocean-Colour Coordinating Group, No. 10; IOCCG: Dartmouth, NS, Canada, 2010; p. 77.
60. Gordon, H.R.; Wang, M. Retrieval of water-leaving radiance and aerosol optical thickness over the oceans with SeaWiFS: A preliminary algorithm. *Appl. Opt.* **1994**, *33*, 443–452. [[CrossRef](#)] [[PubMed](#)]
61. Wang, M.; Shi, W. The NIR-SWIR combined atmospheric correction approach for MODIS ocean color data processing. *Opt. Express* **2007**, *15*, 15722–15733. [[CrossRef](#)] [[PubMed](#)]
62. Wang, M.; Son, S.; Shi, W. Evaluation of MODIS SWIR and NIR-SWIR atmospheric correction algorithms using SeaBASS data. *Remote Sens. Environ.* **2009**, *113*, 635–644. [[CrossRef](#)]
63. Lee, Z.P.; Carder, K.L.; Mobley, C.D.; Steward, R.G.; Patch, J.S. Hyperspectral remote sensing for shallow waters: 2. Deriving bottom depths and water properties by optimization. *Appl. Opt.* **1999**, *38*, 3831–3843. [[CrossRef](#)] [[PubMed](#)]
64. Babin, M.; Stramski, D. Light absorption by aquatic particles in the near-infrared spectral region. *Limnol. Oceanogr.* **2002**, *47*, 911–915. [[CrossRef](#)]
65. International Ocean-Colour Coordinating Group (IOCCG). *Remote Sensing of Inherent Optical Properties: Fundamentals, Tests of Algorithms, and Applications*; Lee, Z., Ed.; Reports of International Ocean-Colour Coordinating Group, No. 5; IOCCG: Dartmouth, NS, Canada, 2006; p. 125.
66. Stramski, D.; Babin, M.; Wozniak, S.B. Variations in the optical properties of terrigenous mineral-rich particulate matter suspended in seawater. *Limnol. Oceanogr.* **2007**, *52*, 2418–2433. [[CrossRef](#)]
67. Wozniak, S.B.; Stramski, D. Modeling the optical properties of mineral particles suspended in seawater and their influence on ocean reflectance and chlorophyll estimation from remote sensing algorithms. *Appl. Opt.* **2004**, *43*, 3489–3503. [[CrossRef](#)] [[PubMed](#)]
68. Shi, W.; Wang, M.H. Characterization of particle backscattering of global highly turbid waters from VIIRS ocean color observations. *J. Geophys. Res. Oceans* **2017**, *122*, 9255–9275. [[CrossRef](#)]
69. Gordon, H.R.; Morel, A. *Remote Assessment of Ocean Color for Interpretation of Satellite Visible Imagery: A Review*; Springer: New York, NY, USA, 1983.
70. Sun, J.; Wang, M. VIIRS reflective solar bands calibration progress and its impact on ocean color products. *Remote Sens.* **2016**, *8*, 194. [[CrossRef](#)]
71. Milliman, J.D.; Shen, H.T.; Yang, Z.S.; Mead, R.H. Transport and deposition of river sediment in the Changjiang estuary and adjacent continental shelf. *Cont. Shelf Res.* **1985**, *4*, 37–45. [[CrossRef](#)]
72. Zhou, W.; Wang, S.; Zhou, Y.; Troy, A. Mapping the concentrations of total suspended matter in Lake Taihu, China, using Landsat-5 TM data. *Int. J. Remote Sens.* **2006**, *27*, 1177–1191. [[CrossRef](#)]

